Kitaev chain in an alternating quantum dot-Andreev bound state array

Miles, Sebastian; Van Driel, David; Wimmer, Michael; Liu, C.

DOI
10.1103/PhysRevB.110.024520

Publication date
2024

Document Version
Final published version

Published in
Physical Review B

Kitaev chain in an alternating quantum dot-Andreev bound state array

Sebastian Miles, David van Driel, Michael Wimmer, and Chun-Xiao Liu *
Qutech and Kavli Institute of Nanoscience, Delft University of Technology, Delft 2600 GA, The Netherlands

(Received 26 October 2023; revised 16 May 2024; accepted 25 June 2024; published 30 July 2024)

We propose to implement a Kitaev chain based on an array of alternating normal and superconductor hybrid quantum dots embedded in semiconductors. In particular, the orbitals in the dot and the Andreev bound states in the hybrid are now on an equal footing, and both emerge as low-energy degrees of freedom in the Kitaev chain, with the couplings being induced by direct tunneling. Due to the electron and hole components in the Andreev bound state, this coupling is simultaneously of the normal and Andreev types, with their ratio being tunable by varying one or several of the experimentally accessible physical parameters, e.g., strength and direction of the Zeeman field, as well as changing the proximity effect on the normal quantum dots. As such, it becomes feasible to realize a two-site Kitaev chain in a simple setup with only one normal quantum dot and one hybrid segment. Interestingly, when scaling up the system to a three-site Kitaev chain, next-nearest-neighbor couplings emerge as a result of high-order tunneling, lifting the Majorana zero energy at the sweet spot. This energy splitting is mitigated in a longer chain, approaching topological protection. Our proposal has two immediate advantages: obtaining a larger energy gap from direct tunneling, and creating a Kitaev chain using a reduced number of quantum dots and hybrid segments.

DOI: 10.1103/PhysRevB.110.024520

I. INTRODUCTION

The Kitaev chain is a toy model comprised of an array of spinless fermions with both normal and Andreev tunnelings between neighboring sites [1]. As a one-dimensional p-wave superconductor, the Kitaev chain in its topological phase will host a pair of Majorana zero modes localized at the end points of the chain [2–13]. These exotic quasiparticles are non-Abelian anyons, i.e., exchanging or braiding two Majoranas will transform between distinct ground-state wave functions in the degenerate manifold [14]. Moreover, since two Majorana modes are spatially separated, quantum information encoded in such a Majorana pair will be more robust against local perturbation and decoherence. With all these intriguing physical properties, Majorana zero modes are regarded as a promising candidate for implementing error-resilient topological quantum computing [15–18].

In solid-state physics, one-dimensional topological superconductivity can be realized in several different types of hybrid materials, e.g., semiconductor-superconductor nanowires [11,19–23], normal channels between planar Josephson junctions [24–26], and ferromagnetic atomic chains on top of a superconductor [27,28]. Despite much experimental progress, a hybrid nanowire is inevitably subject to inhomogeneity and disorder, which can give rise to topologically trivial subgap states [29–35], hindering an unambiguous detection of a topological superconductor. Within this context, a very appealing solid-state platform for implementing a Kitaev chain is based on an array of semiconducting quantum dots [36], which is much more immune to the effect of disorder due to the large level spacing of dot orbitals relative to the disorder fluctuations. In particular, under a sufficiently strong magnetic field, the spin-polarized dot orbitals serve as spinless fermions, coupling with neighboring ones through both normal and Andreev couplings originating from elastic cotunneling (ECT), and crossed Andreev reflection (CAR) mediated by a superconductor. Interestingly, even in a setup of only two quantum dots, a two-site Kitaev chain can be realized and host a pair of poor man's Majorana zero modes at a fine-tuned sweet spot [37].

Very recently, significant experimental progress has been made to transform the above-mentioned theoretical proposals and ideas into a physical realization. In a minimal Kitaev chain device of double quantum dots, the conductance spectroscopies measured at the sweet spot are consistent with the signatures of Majorana zero modes [38]. Here, the key physical insight is to mediate the effective couplings between dot orbitals using Andreev bound states (ABSs) in a semiconductor-superconductor hybrid [39] instead of the continuum states of superconductivity [36,37]. Coupling through an ABS allows that the ratio of CAR and ECT amplitudes can be controlled by varying the chemical potential in the hybrid segment via electrostatic gating [39–42]. This effect was shown to be robust to Coulomb interactions in the dots as well as strong coupling [43]. In spite of progress, current Kitaev chain devices are still suffering from several shortcomings, which may limit their application in quantum technology in the future. First, the excitation energy gap is relatively small ($\sim$25 μeV), due to the fact that CAR and ECT couplings, which are induced by second-order tunneling processes, scale with the tunneling amplitude as $\sim t_0^2/\Delta_0$, with t_0 the characteristic dot-hybrid tunneling strength and Δ_0 the induced gap of an ABS. Second, when scaling up the system into an N-site

*Contact author: chunxiaoliu62@gmail.com

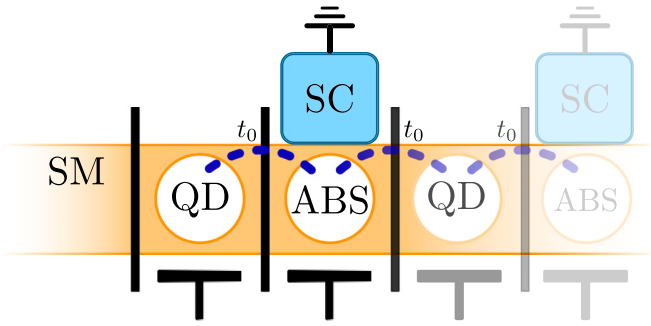

FIG. 1. Schematic of a Kitaev chain device from alternating quantum dots and Andreev bound states created in semiconductor-superconductor hybrids. Quantum dots are formed by confinement potentials induced by tunnel gates (vertical black lines), while the ABS emerges in the quantum dot hosted in the hybrid segment where the semiconductor is proximitized by superconductivity. The tunneling strength (purple dashed lines) between the dot and the ABS can be tuned by varying the voltage of the tunnel gates, and the chemical potentials of the dot and the ABS can be adjusted by changing the plunger gate voltages (black T-elements).

Kitaev chain, one needs to have N quantum dots and $N-1$ pieces of hybrid segments, which makes the device fabrication process increasingly challenging for a longer chain.

Alternatively to using normal quantum dots, Ref. [44] proposed to use Andreev bound states in proximitized quantum dots directly as spinless fermions in a Kitaev chain. There, control over the proximity effect in each quantum dot was required, e.g., by using a quantum point contact to couple to the superconductor.

In the current work, we propose an alternative method to create a Kitaev chain combining the advantages of previous proposals. Our implementation is based on an array of alternating quantum dots and semiconductor-superconductor hybrids (see Fig. 1). In particular, the orbitals in the quantum dots and the ABS in the hybrids are now on an equal footing to the spinless fermions in the Kitaev chain, with the effective couplings being induced by direct tunneling. Due to the electron and hole nature of the ABS, this coupling is simultaneously of the normal and Andreev type, with their ratio being tunable by varying one or several of the experimentally accessible physical parameters, such as the strength and direction of the Zeeman field, as well as changing the tunnel coupling between normal and hybrid quantum dots. As such, it becomes possible to implement a two-site Kitaev chain in a simple setup with only one quantum dot and one hybrid segment, and in general an N-site Kitaev chain requires only N pieces of basic elements of either a dot or a hybrid instead of $2N-1$ as proposed in Ref. [36]. At the same time, our proposal does not require control of the proximity effect in individual dots as in Ref. [44], and it can be realized in the same type of devices as those in previous experiments [39–42]. Moreover, the energy gap of the proposed Kitaev chain will be readily enhanced $\sim t_0$ due to the direct tunneling between the dot and the hybrid. Interestingly, when scaling up the system to a three-site Kitaev chain, next-nearest-neighbor couplings emerge as a result of high-order tunneling, lifting the Majorana zero energy at the sweet spot. Nevertheless, this energy splitting is mitigated in a longer chain, giving a robust zero mode within a larger parameter space, as topological protection is approached.

While our approach is based on alternating normal and hybrid quantum dots, a parallel work considers the case of two superconducting quantum dots showing that a phase difference alone can be used to tune to a sweet spot [45].

The remainder of the work is structured as follows: Section II focuses on the study of a minimal Kitaev chain based on a single pair of quantum dots and ABSs. We introduce the model Hamiltonian in Sec. II A, and we derive its low-energy effective theory in Sec. II B. In particular, in Secs. II C–II E we show how one can systematically fine-tune the sweet spot using experimentally accessible physical parameters, e.g., the strength and direction of the Zeeman field, as well as an induced pairing gap on the quantum dots. In Sec. III, we consider scaling up of the dot-ABS chain, highlighting the emergence of next-nearest-neighbor couplings and the effects on the Majorana properties at the sweet spot. Section IV is devoted to discussions, and we summarize our work in Sec. V.

II. MINIMAL KITAEV CHAIN IN A DOT-ABS PAIR

We first consider a minimal setup comprised of one quantum dot in the normal part and one ABS in the hybrid section. In particular, we derive the effective normal and Andreev couplings between them and the dependence of their ratio on experimentally accessible parameters. Importantly, such a simple setup is sufficient for realizing a two-site Kitaev chain, and it can host poor man's Majorana zero modes at a fine-tuned sweet spot.

A. Model Hamiltonian

The model Hamiltonian for a quantum dot-ABS pair is

$$\begin{aligned} H_{\mathrm{DA}} &= H_D + H_A + H_T, \\ H_D &= (\varepsilon_D + E_{\mathrm{ZD}})n_{D\uparrow} + (\varepsilon_D - E_{\mathrm{ZD}})n_{D\downarrow} + U_D n_{D\uparrow} n_{D\downarrow}, \\ H_A &= (E_A + E_{\mathrm{ZA}})\gamma_{A\uparrow}^\dagger \gamma_{A\uparrow} + (E_A - E_{\mathrm{ZA}})\gamma_{A\downarrow}^\dagger \gamma_{A\downarrow}, \\ H_T &= t_0 \sum_{\sigma,\eta=\uparrow,\downarrow} c_\sigma^\dagger (U_{\mathrm{so}})_{\sigma\eta} d_\eta + \mathrm{H.c.} \end{aligned} \tag{1}$$

Here, H_D is the Hamiltonian for a quantum dot with a single spinful orbital, which is a valid approximation when the dot level spacing is large. $n_{D\sigma} = d_\sigma^\dagger d_\sigma$ is the occupancy number of the dot orbital with spin σ, ε_D is the orbital energy, E_{ZD} is the strength of the induced Zeeman spin splitting, and U_D is the Coulomb energy. H_A is the Hamiltonian of the semiconductor-superconductor hybrid. We assume that the low-energy physics of the hybrid is well described by a pair of subgap ABSs, with all the above-gap continuum states being neglected. $\gamma_{A\sigma} = \sigma u c_\sigma + v c_{\bar{\sigma}}^\dagger$ is the Bogoliubov operator of the ABS with $\sigma = \pm 1$ for spin $\uparrow\downarrow$, and $u^2 = 1 - v^2 = 1/2 + \varepsilon_A/2E_A$ are the BCS coherence factors. $E_A = \sqrt{\varepsilon_A^2 + \Delta_0^2}$ is the excitation energy, ε_A is the normal-state energy, Δ_0 is the induced pairing gap, and E_{ZA} is the strength of the induced Zeeman spin splitting. Here the Zeeman energy for both quantum dots and ABSs is induced by the same globally applied magnetic field, and thereby their spin polarization

axes coincide. However, due to the g-factor renormalization at the semiconductor-superconductor interface [46–48], $E_{\rm ZA}$ can be much weaker than $E_{\rm ZD}$. In our numerical simulations, we set $E_{\rm ZA} = E_{\rm ZD}/2$ without loss of generality. H_T is the tunnel Hamiltonian between the dot and the ABS, with t_0 being the tunneling amplitude, which can be controlled by varying the tunnel gate voltage. $U_{\rm so}$ is a unitary matrix,

$$U_{\rm so} = e^{-i\alpha\sigma_\theta} = \begin{pmatrix} \cos\alpha - i\sin\alpha\sin\theta & -\sin\alpha\cos\theta \\ \sin\alpha\cos\theta & \cos\alpha + i\sin\alpha\sin\theta \end{pmatrix}, \quad (2)$$

with the diagonal and off-diagonal elements denoting the spin-conserving and spin-flipping processes, respectively. Here α is the amount of spin precession accumulated in the tunnel region due to spin-orbit interaction. $\sigma_\theta = \cos\theta\sigma_y + \sin\theta\sigma_z$ is the spin-orbit field, which is perpendicular to the quantum dot chain axis. Without loss of generality, here we have chosen a frame where the magnetic field direction and thus the dot spin polarization axis are fixed, and a rotation of the magnetic field is now equivalently described by rotating the spin-orbit field. In particular, θ is the angle between the magnetic field and the dot chain axis, with $\theta = 0$ ($\theta = \pi/2$) corresponding to being perpendicular (parallel) to the applied magnetic field.

B. Low-energy effective theory and sweet spot conditions

We now derive the low-energy effective theory of the dot-ABS pair introduced in Eq. (1). In the strong Zeeman field regime, the spin-down ABS gets closer to the Fermi energy while the spin-up ABS becomes higher in energy and can be projected away in the leading-order approximation. For the quantum dot, either of the spin-polarized orbitals can be closer to the Fermi energy than the other, depending on the value of the dot's chemical potential. Here, without loss of generality, we restrict our discussions to the spin-down states as the low-energy degrees of freedom in both segments, leaving the discussions of other spin configurations to the Appendix B. Therefore, in the weak tunneling, i.e., $t_0 \ll E_{\rm ZD}, E_{\rm ZA}$, the effective Hamiltonian of a dot-ABS pair is

$$H_{\rm DA}^{\rm eff} \equiv PH_{\rm DA}P = (\varepsilon_D - E_{\rm ZD})d_\downarrow^\dagger d_\downarrow + (E_A - E_{\rm ZA})\gamma_{A\downarrow}^\dagger\gamma_{A\downarrow} - tu\gamma_{A\downarrow}^\dagger d_\downarrow - t_{\rm so}v\gamma_{A\downarrow}d_\downarrow + \text{H.c.}, \quad (3)$$

where P projects the original Hamiltonian onto the spin-down states, t and $t_{\rm so}$ are the tunnel amplitudes for the spin-conserving and spin-flipping processes, respectively, which are defined as

$$t = (U_{\rm so})_{\downarrow\downarrow} = t_0(\cos\alpha + i\sin\alpha\sin\theta),$$
$$t_{\rm so} = (U_{\rm so})_{\downarrow\uparrow} = t_0\sin\alpha\cos\theta, \quad (4)$$

according to Eq. (2). Crucially, because an ABS is a coherent superposition of both electron (u) and hole (v) components, single-electron tunneling from the quantum dot to the hybrid will simultaneously create and annihilate an ABS Bogoliubov excitation, giving both normal and Andreev-like effective couplings

$$t_{\rm eff} = -tu, \quad \Delta_{\rm eff} = -t_{\rm so}v \quad (5)$$

between the dot and the ABS, as shown in Eq. (3). On the other hand, the Hamiltonian for a two-site Kitaev chain is

$$H_{K2} = \varepsilon_1 f_1^\dagger f_1 + \varepsilon_2 f_2^\dagger f_2 + t_{12} f_2^\dagger f_1 + \Delta_{12} f_2 f_1 + \text{H.c.}, \quad (6)$$

where f_i is the annihilation operator of a spinless fermion on site i, ε_i is the on-site energy, and t_{12} and Δ_{12} are the normal and Andreev-like tunneling between adjacent sites. By comparing Eq. (3) with Eq. (6), we obtain the first main finding in the current work, namely that the low-energy physics of a dot-ABS pair in the strong Zeeman regime is a two-site Kitaev chain. In particular, the correspondence between the two is as follows:

$$f_1 \to d_\downarrow, \quad f_2 \to \gamma_{A\downarrow}, \quad \varepsilon_1 \to \varepsilon_D - E_{\rm ZD}, \quad \varepsilon_2 \to E_A - E_{\rm ZA}, \quad t_{12} \to t_{\rm eff} = -tu, \quad \Delta_{12} \to \Delta_{\rm eff} = -t_{\rm so}v. \quad (7)$$

Furthermore, the sweet spot of a two-site Kitaev chain is defined as $\varepsilon_1 = \varepsilon_2 = 0$ and $|t_{12}| = |\Delta_{12}|$. That is, both the dot orbital energy

$$\varepsilon_D - E_{\rm ZD} = 0, \quad (8)$$

and the ABS energy

$$\sqrt{\varepsilon_A^2 + \Delta_0^2} - E_{\rm ZA} = 0, \quad (9)$$

need to be adjusted to be on resonance. In addition, the magnitudes of normal and Andreev-like couplings need to be in perfect balance,

$$|tu| = |t_{\rm so}v|. \quad (10)$$

Once the sweet spot conditions indicated by Eqs. (8)–(10) are all satisfied, a pair of poor man's Majorana zero modes will emerge and localize themselves on the dot and hybrid segments, respectively; see also Fig. 2(d).

C. Tuning Zeeman field strength

We now consider how to reach the sweet spot in a dot-ABS pair by varying experimentally accessible parameters. The most crucial step is the capability of tuning the relative amplitude of $t_{\rm eff}$ and $\Delta_{\rm eff}$. In this subsection, we focus on using the Zeeman field strength as the tuning knob, which means one only varies the strength of the applied magnetic field, with its direction being fixed to be perpendicular to the Rashba spin-orbit field. Setting $\theta = \pi/2$, we thereby have $t = t_0\cos\alpha$ and $t_{\rm so} = t_0\sin\alpha$ in Eq. (4). Among the three sweet spot conditions, the zero-energy dot orbital defined in Eq. (8) can be readily satisfied by merely varying the dot chemical potential. By contrast, the other two defined in Eqs. (9) and (10) are more subtle and mutually constrained. Specifically, under a sufficiently large Zeeman field ($E_{\rm ZA} > \Delta_0$), a zero-energy ABS is obtained only when the normal-state energy is pinned at

$$\varepsilon_A^* \equiv -\sqrt{E_{\rm ZA}^2 - \Delta_0^2} < 0. \quad (11)$$

Note that here we particularly choose the negative ε_A solution, corresponding to a hole-dominant ABS ($u < v$) such that a balance between $t_{\rm eff}$ and $\Delta_{\rm eff}$ indicated in Eq. (10) can be obtained in the weak spin-orbit interaction regime $t_{\rm so} < t$ (a complete overview of all possible sweet spot conditions is

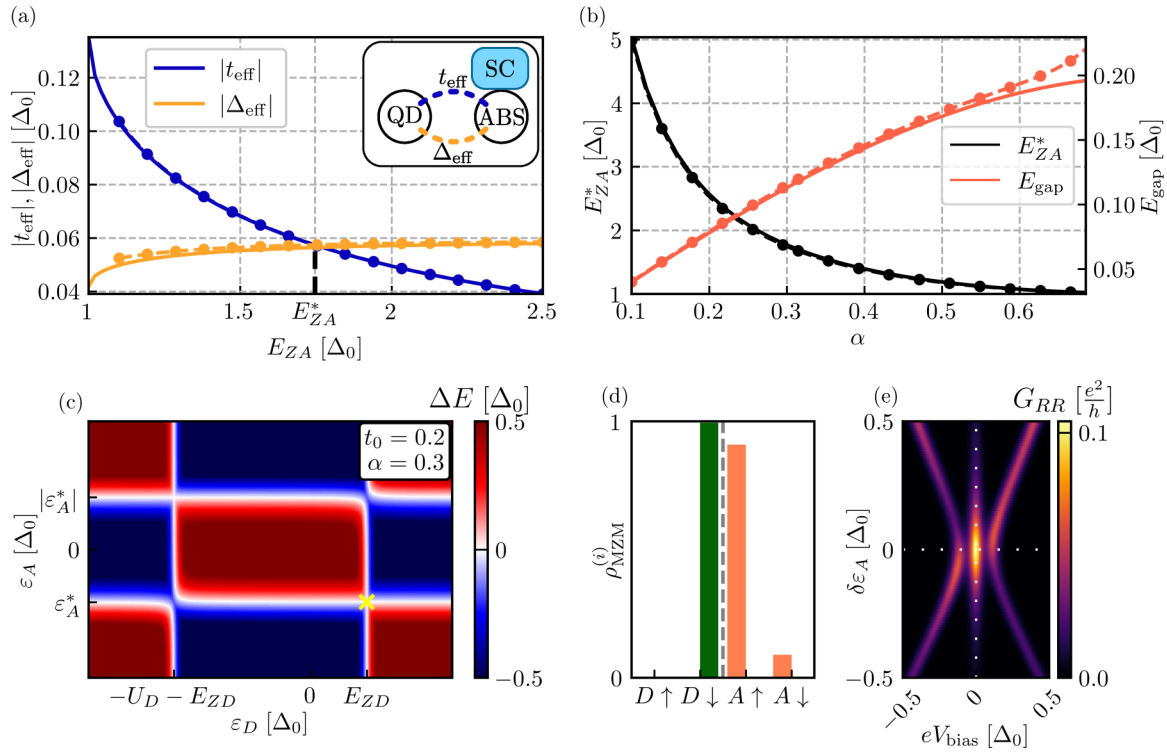

FIG. 2. (a) Strength of the effective couplings $t_{\rm eff}$ and $\Delta_{\rm eff}$ as a function of $E_{\rm ZA}$ in a dot-ABS configuration. Analytic (numerical) results are presented with solid lines (dots). In the numerical calculations, the normal dot Zeeman energy is chosen to be $E_{\rm ZD} = 2E_{\rm ZA}$. At $E_{\rm ZA} = E_{\rm ZA}^*$, we find $|t_{\rm eff}| = |\Delta_{\rm eff}|$. (b) Sweet spot Zeeman energy $E_{\rm ZA}^*$ and excitation gap $E_{\rm gap}$ as a function of α due to spin-orbit interaction. (c) Charge-stability diagram at $E_{\rm ZA} = E_{\rm ZA}^*$. Here $\Delta E = E_{\rm odd,\,gs} - E_{\rm even,\,gs}$ is the energy difference between the ground states in opposite fermion parity subspaces. The sweet spot is indicated by a yellow cross. (d) Majorana wave functions $\rho_{\rm MZM}^{(i)}$ at the sweet spot in (c). (e) Local conductance G_{RR} as a function of bias voltage $V_{\rm bias}$ and ABS detuning $\delta\varepsilon_A$.

given in the Appendix B). As a result, the dependence of the magnitudes of the effective couplings on the Zeeman field strength is as follows:

$$|t_{\rm eff}(E_{\rm ZA})| = \frac{t_0\cos\alpha}{\sqrt{2}}\sqrt{1-\sqrt{1-\Delta_0^2/E_{\rm ZA}^2}},$$
$$|\Delta_{\rm eff}(E_{\rm ZA})| = \frac{t_0\sin\alpha}{\sqrt{2}}\sqrt{1+\sqrt{1-\Delta_0^2/E_{\rm ZA}^2}}. \quad (12)$$

Equations (11) and (12) show that increasing the Zeeman field strength is changing the electron and hole components of the zero-energy ABS, i.e., increasing v from $1/\sqrt{2}$ to close to 1, while decreasing u from $1/\sqrt{2}$ to nearly zero. Therefore, with $E_{\rm ZA}$ increasing from Δ_0, the Andreev coupling $|\Delta_{\rm eff}|$ is enhanced from $t_0\sin\alpha/\sqrt{2}$ to $\sim t_0\sin\alpha$ while the normal coupling $|t_{\rm eff}|$ is suppressed from $t_0\cos\alpha/\sqrt{2}$ to zero in the large Zeeman limit [see Fig. 2(a)]. As a result, in the weak spin-orbit interaction regime ($\alpha < \pi/4$), which is experimentally relevant for InAs and InSb hybrid nanowires [38,40–42], the two coupling strengths will become equal at

$$E_{\rm ZA}^* = \frac{\Delta_0}{\sin(2\alpha)}, \quad (13)$$

as indicated by the black dashed line in Fig. 2(a). Furthermore, the excitation gap at this fine-tuned point is

$$E_{\rm gap} = 2|t_{\rm eff}(E_{\rm ZA}^*)| = t_0\sin(2\alpha), \quad (14)$$

which is defined as twice the effective coupling strength. As shown in Fig. 2(b), $E_{\rm ZA}^*$ is a decreasing function of the spin-orbit interaction strength α, while $E_{\rm gap}$ is increasing. In general, a larger $E_{\rm ZA}^*$ is preferable in order to allow for a wider detuning range of the ABS energy $\delta\varepsilon_A \sim \sqrt{E_{\rm ZA}^{*2} - \Delta_0^2}$. Therefore, in choosing the optimal value of spin-orbit interaction α for the dot-ABS pair, there exists a tradeoff between a sizable gap $E_{\rm gap}$ and a large range of allowed $\delta\varepsilon_A$ for the effective Kitaev model.

To corroborate the analytic results obtained from the low-energy theory, we perform numerical simulations of the dot-ABS pair based on the full many-body Hamiltonian introduced in Eq. (1). In particular, we choose $\Delta_0 = 1$ to be the natural unit, $U_D = 5$, $t_0 = 0.2$, and $\alpha = 0.3$, putting the system into the weak tunneling and weak spin-orbit interaction regime. As shown in Fig. 2(a), the numerically calculated $|t_{\rm eff}|$ and $|\Delta_{\rm eff}|$ as a function of $E_{\rm ZA}$ are in excellent agreement with the analytic results shown in Eq. (12). In Fig. 2(b), the calculated $E_{\rm ZA}^*$ and $E_{\rm gap}$ also match very well with the analytical predictions in Eqs. (13) and (14). Figure 2(c) shows the charge-stability diagram in the $(\varepsilon_D, \varepsilon_A)$ plane. A sweet spot, which is defined as the degeneracy point between even- and odd-parity ground states along with balanced normal and Andreev coupling strengths, appears in the right-bottom corner when $E_{\rm ZA} \approx 1.75\,\Delta_0$, consistent with the analytically predicted value of $E_{\rm ZA}^* = 1.77\,\Delta_0$. Here, the right-bottom corner corresponds to a spin-down dot orbital and a hole-dominant

ABS, which is the focus of this section. Furthermore, the calculated wave functions in Fig. 2(d) show that indeed a pair of Majorana zero modes emerge at the sweet spot [yellow cross in Fig. 2(c)], localized at the quantum dot and hybrid, respectively. In Fig. 2(e), the calculated tunnel conductance spectroscopy in the $(V_{\text{bias}}, \delta\varepsilon_A)$ plane shows a stable zero-bias peak and a parabola-shaped gap peak, consistent with the conductance features of poor man's Majorana zero modes.

D. Tuning Zeeman field direction

We now consider rotating the applied magnetic field in order to find the sweet spot, with the field strength being fixed. Inside the rotation plane, the field direction can be either parallel or perpendicular to the spin-orbit field [49,50]. In our consideration, this field rotation is equivalently described by rotating the spin-orbit field while fixing the Zeeman field and spin polarization axis, as explained after Eq. (2). While increasing field strength changes u and v of the zero-energy ABS, the effect of field rotation is to change the ratio of the spin-conserving t and spin-flipping amplitudes t_{so}, as indicated in Eq. (4). Plugging Eq. (4) into Eq. (5), we thus obtain

$$\begin{aligned} |t_{\text{eff}}(\theta)| &= t_0\sqrt{1-\sin^2\alpha\cos^2\theta}\cdot u(E_{\text{ZA}}),\\ |\Delta_{\text{eff}}(\theta)| &= t_0\sin\alpha\cos\theta\cdot v(E_{\text{ZA}}), \end{aligned} \tag{15}$$

where u and v do not depend on the angle θ. Here we only focus on $0\leqslant\theta\leqslant\pi/2$, since the strength of the effective couplings are π-periodic and symmetric about $\theta=0$. As shown in Fig. 3(a), $|t_{\text{eff}}|$ ($|\Delta_{\text{eff}}|$) is an increasing (decreasing) function of the field angle θ. In particular, when the magnetic field aligns with the spin-orbit field ($\theta=\pi/2$), $|\Delta_{\text{eff}}|$, which is of triplet nature, is suppressed completely due to spin conservation. To obtain a sweet spot in the angle sweep, one thereby needs to start with a sufficiently strong Zeeman field ($E_{\text{ZA}} > E^*_{\text{ZA}}$), giving $|\Delta_{\text{eff}}| > |t_{\text{eff}}|$ at $\theta=0$, and then rotate the magnetic field to reach the balance between $|\Delta_{\text{eff}}|$ and $|t_{\text{eff}}|$. Thus, in general, a larger excitation gap would appear in the vicinity of $\theta=0$, where the spin-flipping processes are maximized.

E. Tuning induced pairing gap in the quantum dot

The third tuning knob we consider in the current work is the superconducting pairing gap in the normal quantum dot, which can be induced from the adjacent hybrid by the proximity effect. Microscopically, this proximity effect can originate from either the ABS or the continuum states, with the forms being

$$\begin{aligned} \Delta_{\text{ABS}} &= \left(t^2+t_{\text{so}}^2\right)\frac{uv}{E_A+E_{\text{ZA}}},\\ \Delta_{\text{cont}} &= \left(t^2+t_{\text{so}}^2\right)\frac{\chi}{\Delta_0}, \end{aligned} \tag{16}$$

up to the leading order. Here Δ_{ABS} comes from the high-energy spin-up ABS, while Δ_{cont} is obtained assuming a zero-bandwidth model for the continuum states, with χ characterizing the continuum density of states, which can be quite different from the ABS. Since both Δ_{ABS} and Δ_{cont} increase with the tunnel amplitude t_0, their strength can be experimentally enhanced by lowering the tunnel barrier between the dot and the hybrid. In the following calculations, we do not distinguish between the microscopic origins of the proximity effect. We consider instead their combined effect in a phenomenological way (examples of a microscopic model to change the induced superconductivity by tuning t_0 are given in the Appendix D). Now the dot Hamiltonian becomes

$$H_D' = H_D + H_{\text{ind}}, \quad H_{\text{ind}} = \Delta_D d_\uparrow^\dagger d_\downarrow^\dagger + \text{H.c.}, \tag{17}$$

where H_D is the bare dot Hamiltonian defined in Eq. (1), and Δ_D is the total induced gap on the dot. As a result, the dot orbital in the quantum dot is now proximitized into a Yu-Shiba-Rusinov state [51–54], with the electron and hole components being

$$\begin{aligned} u_D &= \sqrt{\frac{1}{2}+\frac{\xi_D}{2(U_D/2+E_{\text{ZD}})}} \approx 1-\frac{1}{8}\left(\frac{\Delta_D}{U_D/2+E_{\text{ZD}}}\right)^2,\\ v_D &= \sqrt{\frac{1}{2}-\frac{\xi_D}{2(U_D/2+E_{\text{ZD}})}} \approx \frac{1}{2}\left(\frac{\Delta_D}{U_D/2+E_{\text{ZD}}}\right), \end{aligned} \tag{18}$$

where

$$\xi_D \equiv \varepsilon_D + U_D/2 = \sqrt{\left(\frac{U_D}{2}+E_{\text{ZD}}\right)^2-\Delta_D^2} \tag{19}$$

is determined by the zero-energy condition for the bound state. Note that the approximations in Eq. (18) are made in the weak proximity effect regime ($\Delta_D \ll U_D$), and thereby, up to the leading order of Δ_D/U_D, $u_D=1$ becomes a constant and only $v_D \propto \Delta_D$ grows linearly with Δ_D. As a result, the

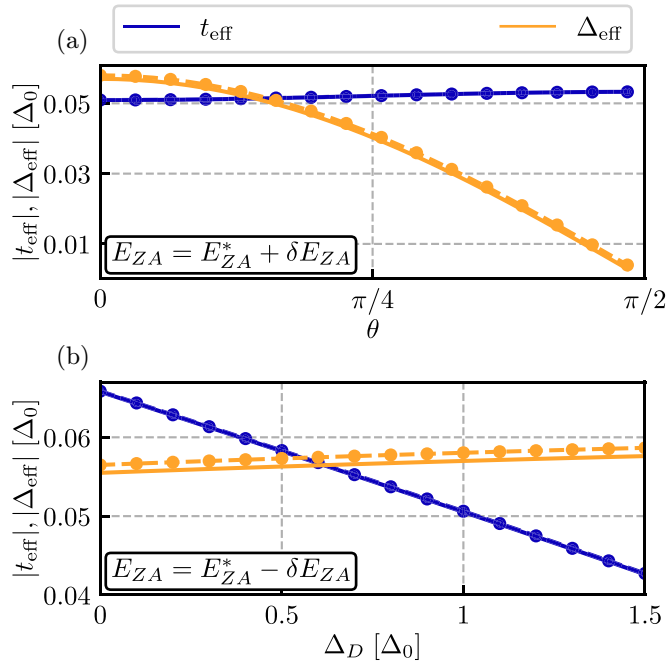

FIG. 3. (a) Strength of the effective couplings $|t_{\text{eff}}|$ and $|\Delta_{\text{eff}}|$ as a function of the field angle θ at $E_{\text{ZA}} = E^*_{\text{ZA}} + \delta E_{\text{ZA}}$ ($\delta E_{\text{ZA}} = 0.2$). Here θ is the angle between the magnetic field and the dot chain axis, and in particular, $\theta=0$ corresponds to the magnetic field being perpendicular to the spin-orbit field. (b) $|t_{\text{eff}}|$ and $|\Delta_{\text{eff}}|$ as a function of induced gap Δ_D at $E_{\text{ZA}} = E^*_{\text{ZA}} - \delta E_{\text{ZA}}$. In both scenarios, a perfect balance between $|t_{\text{eff}}|$ and $|\Delta_{\text{eff}}|$ can be obtained.

effective couplings between the dot and the ABS become

$$t_{\text{eff}} = t(u_A u_D - v_A v_D) \approx t(u_A - v_A v_D),$$
$$\Delta_{\text{eff}} = t_{\text{so}}(v_A u_D + u_A v_D) \approx t_{\text{so}}(v_A + u_A v_D). \quad (20)$$

That is, t_{eff} decreases with the magnitude of the induced pairing, while Δ_{eff} increases with it. In Fig. 3(b), the solid lines show the analytic curves of $|t_{\text{eff}}|$ and $|\Delta_{\text{eff}}|$ as a function of Δ_D derived in Eq. (20), which agree with the numerical results obtained from the full many-body Hamiltonian (dots and dashed lines). Note that here the Zeeman field is perpendicular to the spin-orbit field, and its strength is chosen to be $E_{\text{ZA}} < E^*_{\text{ZA}}$ such that $|t_{\text{eff}}| > |\Delta_{\text{eff}}|$ at zero proximity effect, and a balance between them is reached at a sufficiently strong Δ_D.

III. SCALING UP THE KITAEV CHAIN

We now go beyond the minimal setup of a dot-ABS pair and scale up the system into a longer chain. Without loss of generality, we consider tuning up the sweet spot and Majorana modes by varying the Zeeman field strength, with its direction being fixed to be perpendicular to the spin-orbit field and no superconducting proximity effect on normal quantum dots. Moreover, we assume homogeneity in the long-chain system, i.e., all the physical parameters for the dots/ABS/tunneling are identical.

A. Three-site Kitaev chain: Dot-ABS-dot

As a first example of the three-site Kitaev chain, we consider a dot-ABS-dot chain, focusing on its physical properties around the sweet spot. The Hamiltonian is given by

$$H_{\text{DAD}} = H_{\text{DL}} + H_A + H_{\text{DR}} + H_{\text{TLA}} + H_{\text{TRA}}, \quad (21)$$

where H_{DL}, H_A, and H_{DR} are the Hamiltonians for the left dot, the middle ABS, and the right dot, respectively. H_{TLA} (H_{TRA}) is tunnel Hamiltonian between the ABS and the left (right) dot. The specific forms of these individual Hamiltonian terms are the same as those introduced in Eq. (1). Under the assumption of homogeneity, one can simultaneously tune both dot-ABS pairs into their own sweet spot by applying a global Zeeman field $E_{\text{ZA}} = E^*_{\text{ZA}}$ and setting $\varepsilon_{\text{DL}} = \varepsilon_{\text{DR}} = \varepsilon^*_D$ and $\varepsilon_A = \varepsilon^*_A$ as indicated in Fig. 2(c), such that the whole system is automatically entering the sweet spot regime. Indeed, as shown in Fig. 4(a), two unpaired Majorana modes are completely localized on the outermost quantum dots, precisely as expected for the sweet spot of a three-site Kitaev chain [1]. However, a surprising fact is that the energy of the two Majoranas is split into $E_{\text{MZM}} \approx 0.01$, which is approximately one-tenth of the excitation gap [see Fig. 4(b) at $\delta\varepsilon = 0$], even though there is no wave function overlap between them at all [see Fig. 4(a)]. Furthermore, as shown in Fig. 4(b), the energy spectrum of the whole system as a function of the detuning energy deviates from the cubic scaling behavior $E \propto (\delta\varepsilon)^3$ of an idealized three-site Kitaev chain. Here the detuning energy is defined as $\delta\varepsilon = \varepsilon_{\text{DL}} - \varepsilon^*_D = \varepsilon_{\text{DR}} - \varepsilon^*_D = \varepsilon_A - \varepsilon^*_A$.

To understand the physical mechanism underlying this intriguing energy splitting, we develop a low-energy effective theory for the dot-ABS-dot chain, including both the first- and second-order contributions,

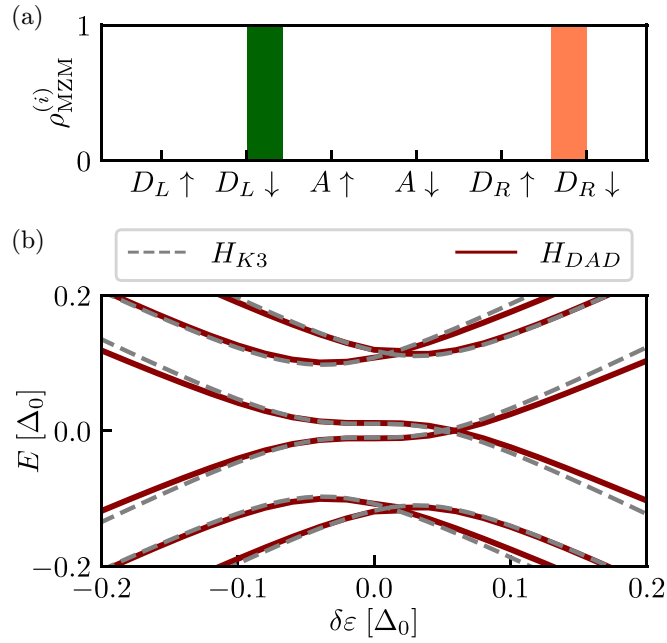

FIG. 4. (a) Majorana wave functions at the sweet spot of a dot-ABS-dot chain. (b) Energy spectrum of the system as a function of detuning energy $\delta\varepsilon$. The solid lines are calculated for the full many-body Hamiltonian, while the gray dashed lines are based on the low-energy effective theory. The energy splitting at $\delta\varepsilon = 0$ is due to effective next-nearest-neighbor coupling between the two outer dots.

$$H_{\text{DAD,eff}} = H^{(1)}_{\text{DAD,eff}} + H^{(2)}_{\text{DAD,eff}}. \quad (22)$$

Here $H^{(1)}_{\text{DAD,eff}}$ includes only the low-energy states and direct tunneling terms, which is a straightforward generalization of the dot-ABS pair, giving

$$\begin{aligned} H^{(1)}_{\text{DAD,eff}} &= PH_{\text{DAD}}P \\ &= (\varepsilon_{\text{DL}} - E_{\text{ZD}})d^\dagger_{L\downarrow}d_{L\downarrow} + (E_A - E_{\text{ZA}})\gamma^\dagger_{A\downarrow}\gamma_{A\downarrow} \\ &\quad + (\varepsilon_{\text{DR}} - E_{\text{ZD}})d^\dagger_{R\downarrow}d_{R\downarrow} + t_{\text{eff}LA}\gamma^\dagger_{A\downarrow}d_{L\downarrow} \\ &\quad + \Delta_{\text{eff}LA}\gamma_{A\downarrow}d_{L\downarrow} + t_{\text{eff}RA}\gamma^\dagger_{A\downarrow}d_{R\downarrow} \\ &\quad + \Delta_{\text{eff}RA}\gamma_{A\downarrow}d_{R\downarrow} + \text{H.c.} \end{aligned} \quad (23)$$

Indeed, the first-order effective Hamiltonian $H^{(1)}_{\text{DAD,eff}}$ is a three-site Kitaev chain. In particular, the sweet spot is reached when all the on-site energies are zero and $E_{\text{ZA}} = E^*_{\text{ZA}}$, giving $t_{\text{eff}LA} = t_{\text{eff}RA} = \Delta_{\text{eff}LA} = \Delta_{\text{eff}RA}$. In addition, unlike the dot-ABS pair, we now also include the second-order perturbation terms in the effective Hamiltonian as follows:

$$\begin{aligned} H^{(2)}_{\text{DAD,eff}} &= PH_T\frac{1-P}{H_A}H_TP \\ &= t_{DD}d^\dagger_{L\downarrow}d_{R\downarrow} + \Delta_{DD}d_{L\downarrow}d_{R\downarrow} + \text{H.c.}, \end{aligned} \quad (24)$$

where $H_T = H_{\text{TLA}} + H_{\text{TRA}}$. Equation (24) indicates that effective next-nearest-neighbor couplings between the outer dots can be mediated by the high-energy ABS in the hybrid via second-order tunnelings (see Fig. 5). Specifically, these

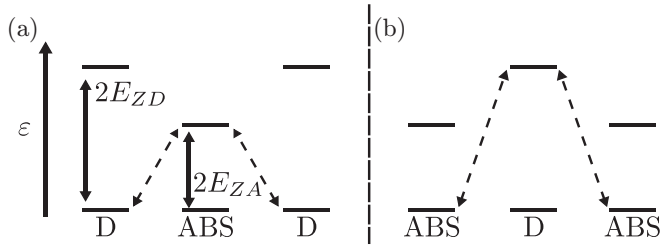

FIG. 5. Schematic of the second-order tunneling processes that are responsible for the next-nearest-neighbor couplings in a dot-ABS-dot or ABS-dot-ABS chain.

couplings have the following form:

$$t_{DD} = \frac{t^2v^2 + t_{so}^2u^2}{2E_{ZA}} \approx \frac{t^2v^2}{2E_{ZA}},$$
$$\Delta_{DD} = \frac{2tt_{so}uv}{2E_{ZA}} \ll t_{DD}, \tag{25}$$

where we assume that the weak spin-orbit limit $t_{so} \ll t$ and $u \ll v$ holds in the vicinity of the sweet spot. Therefore, up to the second order in t_0, the low-energy physics of a dot-ABS-dot chain is well described by a generalized three-site Kitaev chain,

$$H_{K3} = \sum_{i=1}^{3} \varepsilon_i f_i^\dagger f_i + \sum_{i=1}^{2} (t f_{i+1}^\dagger f_i + \Delta f_{i+1} f_i)$$
$$+ t_{31} f_3^\dagger f_1 + \Delta_{31} f_3 f_1 + \text{H.c.}, \tag{26}$$

where f_i is the spinless fermion on the ith site, ε_i is the on-site energy, t and Δ are the normal and Andreev tunnelings between adjacent sites, and t_{31} and Δ_{31} are the next-nearest-neighbor tunnelings. Indeed, as shown in Fig. 4(b), the energy spectrum of the full many-body Hamiltonian in Eq. (21) is in excellent agreement with that of the effective model in Eq. (26), supporting our perturbation theory analysis. In the calculation of the generalized Kitaev model, the Hamiltonian parameters are chosen as $t = \Delta = t_{\text{eff}}(E_{ZA}^*)$, $t_{31} = t_{DD}$, $\Delta_{31} = 0$, and $\varepsilon_i = \delta\varepsilon$. Therefore, our new finding here is that even though the two Majorana modes have no wave-function overlap in space at the sweet spot [see Fig. 4(a)], they are still coupled to each other via next-nearest-neighbor couplings, giving a finite-energy splitting [see Fig. 4(b)]. In Appendix E, we expand our discussion to the case of inhomogeneities of g-factors and spin-orbit interaction between the constituent dots of the array.

B. Three-site Kitaev chain: ABS-dot-ABS

We briefly discuss the physics of an ABS-dot-ABS chain, which is somewhat dual to a dot-ABS-dot chain. The Hamiltonian is given by

$$H_{\text{ADA}} = H_{\text{AL}} + H_D + H_{\text{AR}} + H_{\text{TLD}} + H_{\text{TRD}}, \tag{27}$$

which has two outer ABSs connected by a quantum dot in the middle. Similar to the analysis performed in the previous subsection, the low-energy physics of the system is

$$H_{\text{ADA,eff}} = H_{\text{ADA,eff}}^{(1)} + H_{\text{ADA,eff}}^{(2)}, \tag{28}$$

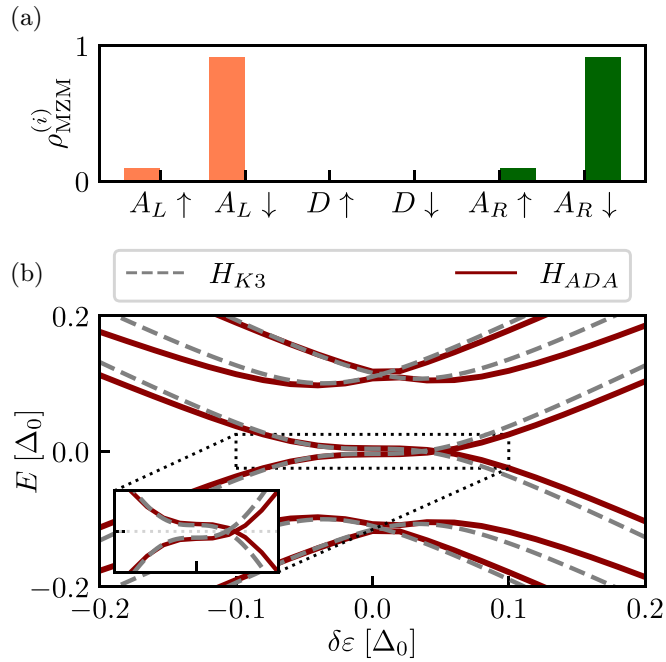

FIG. 6. (a) Majorana wave functions at the sweet spot of an ABS-dot-ABS chain. (b) Energy spectrum of the system as a function of detuning energy $\delta\varepsilon$. The solid lines are calculated for the full many-body Hamiltonian, while the gray dashed lines are based on the low-energy effective theory. The energy splitting at $\delta\varepsilon = 0$ is due to effective next-nearest-neighbor coupling between the two outer ABS.

where the first-order term is

$$H_{\text{ADA,eff}}^{(1)} = (E_{\text{AL}} - E_{\text{ZA}})\gamma_{L\downarrow}^\dagger\gamma_{L\downarrow} + (\varepsilon_D - E_{\text{ZD}})d_\downarrow^\dagger d_\downarrow$$
$$+ (E_{\text{AR}} - E_{\text{ZA}})\gamma_{R\downarrow}^\dagger\gamma_{R\downarrow} + t_{\text{effLD}}d_\downarrow^\dagger\gamma_{L\downarrow} + \Delta_{\text{effLD}}d_\downarrow\gamma_{L\downarrow}$$
$$+ t_{\text{effRD}}d_\downarrow^\dagger\gamma_{R\downarrow} + \Delta_{\text{effRD}}d_\downarrow\gamma_{R\downarrow} + \text{H.c.}, \tag{29}$$

and the second-order term is

$$H_{\text{ADA,eff}}^{(2)} = t_{AA}\gamma_{L\downarrow}^\dagger\gamma_{R\downarrow} + \Delta_{AA}\gamma_{L\downarrow}\gamma_{R\downarrow} + \text{H.c.}, \tag{30}$$

with

$$t_{AA} = \frac{t^2v^2 + t_{so}^2u^2}{2E_{\text{ZD}}} \approx \frac{t^2v^2}{2E_{\text{ZD}}},$$
$$\Delta_{AA} = \frac{2tt_{so}uv}{2E_{\text{ZD}}} \ll t_{AA}. \tag{31}$$

We thus see that the low-energy physics of an ABS-dot-ABS chain is also a generalized three-site Kitaev chain, with only the roles of quantum dots and ABSs being interchanged. Actually the sweet spot of the system is also reached at $E_{\text{ZA}} = E_{\text{ZA}}^*$, giving an excitation energy gap of a similar size with its dual system. The only difference is a more suppressed Majorana energy splitting [see Fig. 6(b)] because a larger Zeeman spin splitting in the quantum dot suppresses the second-order tunnelings, as indicated in Eq. (31). As for the dot-ABS-dot setup, in Appendix E we expand the discussion to situations in which the dots have inhomogeneities in either g-factors or spin-orbit interaction. In particular, we find that the

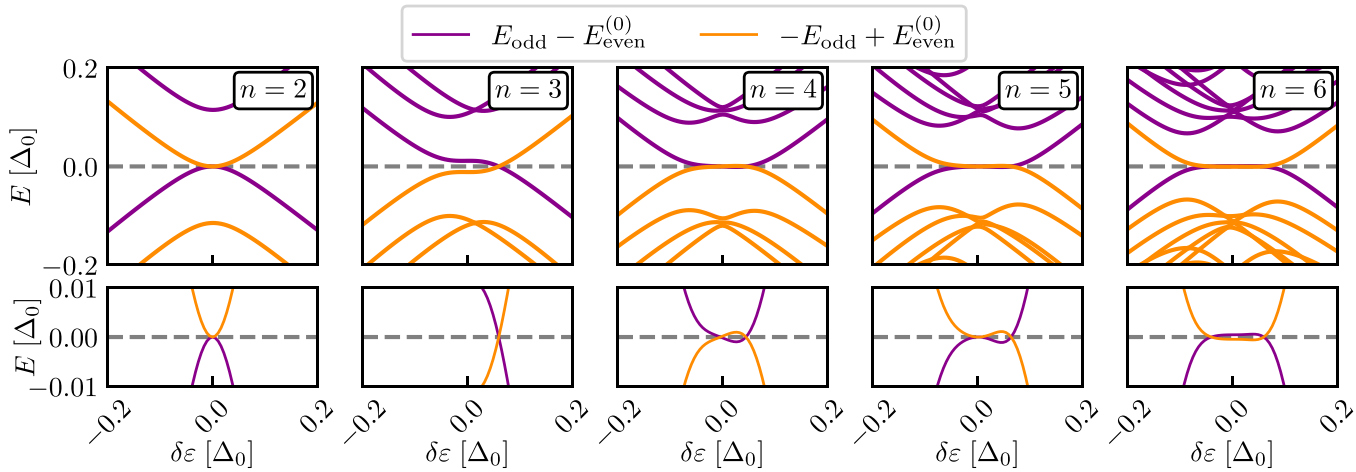

FIG. 7. Energy spectra of N-site alternating quantum dot-ABS chains around the sweet spot. For intermediate length chains (e.g., $N = 3$), the next-nearest-neighbor coupling has an appreciable effect on the Majorana energy splitting at the sweet spot. As the chain is further scaled up ($N \geqslant 4$), this Majorana energy splitting is quickly suppressed due to the short-range nature of this effective coupling, as shown in Eq. (33).

ABS-dot-ABS system yields more resilient sweet spots due to the larger separation of levels on the central normal dot.

C. Longer Kitaev chain

For a general Kitaev chain with N alternating quantum dots and ABSs in total, its low-energy physics can be well described by an effective Hamiltonian up to the $(N-1)$th order, i.e.,

$$H_{N,\rm eff} = \sum_{k=1}^{N-1} H^{(k)}_{N,\rm eff}. \tag{32}$$

In particular, the strength of the effective couplings between two arbitrary sites in such an N-site chain has the following scaling behavior:

$$\Gamma_k \sim \frac{t_0^k}{(2E_Z)^{k-1}} \sim t_0 \exp\{-(k-1)\log(2E_Z/t_0)\} \tag{33}$$

for $1 \leqslant k \leqslant N-1$. Here Γ_k denotes the effective normal or Andreev coupling between any two sites separated by a distance of k (e.g., Γ_1 for the nearest-neighbor coupling), and E_Z is the Zeeman spin splitting of either the dot or the ABS located between the two sites considered. Physically, Γ_k originates from virtual tunnelings that include k times of single-electron tunneling events via $k-1$ different high-energy states that are gapped from the Fermi energy due to Zeeman spin splitting. From Eq. (33), we see that Γ_k decays exponentially with the distance between the coupled two sites, with the decay length being approximately

$$\xi_\Gamma^{-1} \sim \log(2E_Z/t_0). \tag{34}$$

The range of the effective couplings thus decreases with an increase of Zeeman energy in the dot-ABS chain, and as a result, the low-energy physics of the dot-ABS chain will asymptotically approach the idealized spinless Kitaev chain only in the large Zeeman energy limit ($E_Z \gg t_0$). Another crucial feature of Γ_k is being short-ranged in nature, making it possible to reach topological protection in the long-chain limit. Indeed, the numerical simulations based on the full many-body Hamiltonian for the N-site dot-ABS chain (see Fig. 7) show that the finite Majorana energy splitting become strongly suppressed to nearly zero once there are as many as four or five sites. Moreover, for N as large as six, the range of $\delta\varepsilon$ for hosting zero-energy excitation extends asymptotically to the long-wire limit $-t_{\rm eff}(E^*_{\rm ZA}) \lesssim \delta\varepsilon \lesssim t_{\rm eff}(E^*_{\rm ZA})$, and signatures of gap closing and reopening begin to appear near $|\delta\varepsilon| \sim t_{\rm eff}$, indicating the emergence of a topological phase transition.

IV. DISCUSSION

In the current work, we proposed an alternative way of implementing a Kitaev chain in an alternating quantum dot-Andreev bound state array. Although the configuration of the proposed hybrid devices resembles those considered in Refs. [36,37,39,43], a fundamental difference is the role of ABSs. In Refs. [39,43], the ABSs are *gapped* and only serve as a virtual coupler to mediate the effective couplings between quantum dots. By contrast, here the spin-polarized ABS is taken close to the Fermi energy and is on an equal footing with the dot orbitals as the spinless fermions. Consequently, an immediate advantage of our proposal is to emulate a Kitaev chain using a reduced number of quantum dots and hybrid segments in a device. In particular, it becomes possible to implement a two-site Kitaev chain and poor man's Majoranas using only one quantum dot and one hybrid segment. Furthermore, the existing two-site Kitaev chain device comprised of a double quantum dot linked by a hybrid [38] is now suitable for realizing a three-site Kitaev chain exhibiting the physics of bulk-edge correspondence in the vicinity of its sweet spot. On the other hand, our proposal differs from the ABS chain proposed in Ref. [44] in that we require only half the number of superconducting leads, and we do not need to control the quantum point contact between the semiconductor wire and the superconductor leads, making our theoretical proposal more experimentally accessible. Another advantage of our proposal is the ability to obtain a relatively large excitation gap, because now the effective couplings originate from direct couplings of the dot-ABS pair, i.e., $E_{\rm gap} \sim t_0$, in stark contrast

with the second-order tunneling processes $E_{\rm gap} \sim t_0^2/\Delta_0$ in previous work [39].

Throughout the work, we have assumed perfect homogeneity when considering a long Kitaev chain device ($N \geqslant 3$), but this has to be relaxed in a realistic device. That is, the quantum dots can have different values of charging energy U_D, g-factor $E_{\rm ZD}$, while $E_{\rm ZA}$ and the induced gap Δ_0 of the ABS may vary from piece to piece. Therefore, it would be rather unlikely to drive the whole long chain into the sweet spot by merely controlling a global magnetic field, and as a result, the tuning knob of the induced gap on the quantum dots becomes particularly crucial, because it will allow for fine-tuning the couplings in each individual dot-ABS pair into perfect balance.

Another finding of our work is the presence of couplings beyond the nearest neighbors, which originate from high-order tunneling processes. Their effect will be most prominent in a three-site device (e.g., a dot-ABS-dot chain), where the Majorana energy at the sweet spot becomes split, even though their wave functions are completely separated on the outermost dots. This raises a new question of whether it is possible to define such a sweet spot that simultaneously satisfies three conditions: (i) complete spatial separation of the Majoranas, (ii) robustness against on-site-energy detuning, and (iii) minimizing the Majorana energy to nearly zero. To obtain an idealized Kitaev chain model, as shown in Eqs. (25) and (31), the couplings between two distant sites would be suppressed in the strong Zeeman limit, similar to the findings in the Majorana nanowire scenarios [55]. In addition, in the tunneling regime $t_0 \ll E_Z$, such couplings are short-ranged in nature, and therefore the effect will be mitigated as the number of sites is scaled up. As we show, when the number of sites is as large as six, the whole chain becomes very close to a topological Kitaev chain with robust zero energy and signatures of gap closing and reopening near the quantum phase transition.

V. SUMMARY

To summarize, we have proposed an alternative route to simulating a Kitaev chain in an alternating quantum dot-Andreev bound state array. In particular, both the dot orbitals and the ABS are now on an equal footing as spinless fermions, and the relative amplitude of normal and Andreev couplings between adjacent sites, are highly tunable by the strength and direction of the magnetic field, as well as the magnitude of the induced pairing gap on quantum dots. As the quantum dot-ABS chain is scaled up, couplings beyond the nearest neighbors emerge, affecting the Majorana energy at the sweet spot. Nonetheless, due to the short-range nature of these couplings, topological protection of Majorana zero modes will recover in the long chain limit. Our proposal will allow for a more efficient simulation of an artificial Kitaev chain using a reduced number of quantum dots or hybrid segments, and at the same time it will enable us to obtain a larger excitation gap above the Majorana zero modes. In recent experiments [40,56], it was shown to be possible to isolate a single ABS in a short hybrid region, making our proposal particularly appealing and relevant to the ongoing studies.

All codes related to the results of the present manuscript can be found in the accompanying Zenodo repository [57].

Note added. We have been made aware of Ref. [45] by its authors. In contrast to [45], we consider the limit of both quantum dots being maximally asymmetric in their proximity coupling to the superconductor.

ACKNOWLEDGMENTS

We are particularly grateful to S. L. D. ten Haaf and B. Roovers for sharing and discussing experimental data with us, motivating this work. We further thank A. M. Bozkurt, J. D. Torres Luna, and K. Vilkelis for useful theory discussions. We are grateful to the authors of [45] for making us aware of their work prior to publication. This work was supported by a subsidy for top consortia for knowledge and innovation (TKI toeslag), by the Dutch Organization for Scientific Research (NWO). S.M. acknowledges funding of NWO through OCENW.GROOT.2019.004.

S.M. and C.-X.L. contributed equally to this work. C.-X.L. formulated the project idea and designed the project with input from D.v.D. and M.W. S.M. and C.-X.L. performed the calculations. S.M. generated the figures with input from C.-X.L. C.-X.L. and M.W. supervised the project. All authors discussed the results and contributed to the writing of the manuscript.

APPENDIX A: DETAILS OF THE NUMERICAL CALCULATIONS

The numerical results in this work are obtained by exact diagonalization of the full many-body Hamiltonian, e.g., Eq. (1), in Fock space. The dimension of the total Hamiltonian is 2^{2N}, where N is the number of quantum dots plus ABS in the chain. Due to fermion parity conservation, we can decompose the Hamiltonian into even- and odd-parity subspace of dimension 2^{2N-1}. As a result, the excitation energy E, as depicted in Figs. 4, 6, and 7, has been obtained through

$$E_\lambda = E^{(\lambda)}_{\rm odd} - E^{(0)}_{\rm even} \tag{A1}$$

for $\lambda = 0, 1, 2, \ldots, 2^{2N-1} - 1$. In a similar fashion, ΔE in the charge-stability diagrams, as depicted in Fig. 2(c), is obtained by restricting λ in Eq. (A1) to $\lambda = 0$. To obtain $t_{\rm eff}$ and $\Delta_{\rm eff}$, we make use of the following relation:

$$\begin{aligned} \Delta_{\rm eff} &= (E_1 + E_0)/2, \\ t_{\rm eff} &= (E_1 - E_0)/2, \end{aligned} \tag{A2}$$

where E_0, E_1 are defined in Eq. (A1).

Here $t_{\rm eff}$ is related to the cost of exciting an unpaired electron while $\Delta_{\rm eff}$ is related to splitting the lowest Cooper pair into two unpaired electrons. The gap energy, depicted in, e.g., Fig. 2(b), is obtained directly through

$$E_{\rm gap} \equiv E_1. \tag{A3}$$

In addition, the spectrum plots also contain the energy of the MZM itself in the lowest-lying line following

$$E_{\rm MZM} \equiv E_0. \tag{A4}$$

The Zeeman energies characterizing the sweet spot depicted in Fig. 2(b) have been determined by using the properties of the CSD [see Fig. 2(c)]. As Fig. 3 shows, if $E_{\rm ZA}$ is slightly

below the sweet spot E^*_{ZA}, the degeneracy crossing vanishes in favor of an t_{eff} dominated ($\Delta E > 0$) anticrossing. For $E_{\mathrm{ZA}} > E^*_{\mathrm{ZA}}$, the same anticrossing is caused by a dominating Δ_{eff} process ($\Delta E < 0$). Therefore, the sweet spot is characterized by the root $\Delta E(E^*_{\mathrm{ZA}}) = 0$ at the point where the charge degeneracy lines have their smallest distance in the $(\varepsilon_D, \varepsilon_A)$ plane. To determine the point of minimal distance, we perform a transformation of the chemical potentials into polar coordinates,

$$(\varepsilon_D, \varepsilon_A) \to (r_\varepsilon \cos(\varphi_\varepsilon), r_\varepsilon \sin(\varphi_\varepsilon)) \quad r_\varepsilon = \sqrt{\varepsilon_D^2 + \varepsilon_A^2},$$
$$\tan(\varphi_\varepsilon) = \varepsilon_A/\varepsilon_D. \tag{A5}$$

In polar coordinates, the point with minimal distance between the degeneracy lines is found to satisfy

$$(r_\varepsilon, \varphi_\varepsilon) \in \{r_\varepsilon, \varphi_\varepsilon : \min[\Delta E(r_\varepsilon, \varphi_\varepsilon)] \wedge \max[\Delta E(r_\varepsilon, \varphi_\varepsilon)]\}. \tag{A6}$$

The bottom right corner we discuss has the further constraint that $\varphi_\varepsilon \in [-\pi/2, 0]$. To obtain the MZM wave functions, $\rho^{(i)}_{\mathrm{MZM}}$, depicted in Figs. 2, 4, 6, we define the spin-dependent on-site MZM operators

$$w_\sigma = (d_\sigma + d_\sigma^\dagger), \tag{A7}$$

$$z_\sigma = i(d_\sigma - d_\sigma^\dagger). \tag{A8}$$

The MZM on the ABS are defined analogously with the corresponding creation and annihilation operators. From Eq. (A7) we find the MZM wave functions through

$$\rho^{(w)}_{\mathrm{MZM}} = \left|\langle\psi^{(0)}_{\mathrm{odd}}|w_\sigma + w_{\bar\sigma}|\psi^{(0)}_{\mathrm{even}}\rangle\right|^2, \tag{A9}$$

$$\rho^{(z)}_{\mathrm{MZM}} = \left|\langle\psi^{(0)}_{\mathrm{odd}}|z_\sigma + z_{\bar\sigma}|\psi^{(0)}_{\mathrm{even}}\rangle\right|^2, \tag{A10}$$

where $|\psi^{(\lambda)}\rangle$ denotes an eigenstate of the many-body Hamiltonian; cf. Eq. (1). The conductance plot in Fig. 2(e) has been obtained by implementing the rate equations listed in the supplemental material of [43]. The energies of the Kitaev model [1] in Figs. 4 and 6 have been obtained by exact diagonalization and replacing the parameters by their corresponding partners from perturbation theory; cf. Eq. (7). Lastly, the perturbative analysis has been performed in part by using Pymablock [58]. All codes related to the results presented in the manuscript can be found in the accompanying Zenodo repository [57].

APPENDIX B: SYMMETRIES OF THE CHARGE-STABILITY DIAGRAM

The CSD depicted in Fig. 2 shows six distinct regions with alternating ground-state properties. If the low-energy subspace is described by the Hamiltonian given in Eq. (3), then varying the chemical potentials ε_i on the two sites changes the charge state of the dots. The possible charge states on each site depending on the chemical potential are

$$|\downarrow\uparrow\rangle, \quad \varepsilon_D < -U_D - E_{\mathrm{ZD}}, \tag{B1}$$
$$|\downarrow\rangle, \quad -U_D - E_{\mathrm{ZD}} < \varepsilon_D < E_{\mathrm{ZD}}, \tag{B2}$$
$$|0\rangle, \quad \varepsilon_D > E_{\mathrm{ZD}} \tag{B3}$$

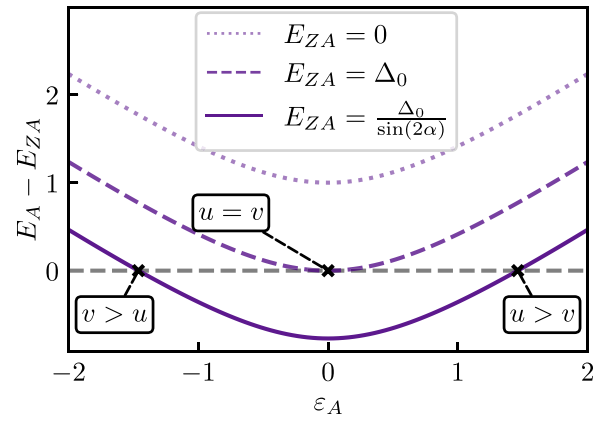

FIG. 8. ABS energy depending on the on-site chemical potential of the ABS dot for varying Zeeman energies E_{ZA}. Depending on the Zeeman energy, at most two ABS solutions will become available to potentially host sweet spots of the system.

on the normal dot, and

$$u|0\rangle + v|\uparrow\downarrow\rangle, \quad \varepsilon_A < -\sqrt{E^2_{\mathrm{ZA}} - \Delta_0^2}, \tag{B4}$$

$$|\downarrow\rangle, \quad -\sqrt{E^2_{\mathrm{ZA}} - \Delta_0^2} < \varepsilon_A < \sqrt{E^2_{\mathrm{ZA}} - \Delta_0^2}, \tag{B5}$$

$$u|0\rangle + v|\uparrow\downarrow\rangle, \quad \varepsilon_A > \sqrt{E^2_{\mathrm{ZA}} - \Delta_0^2} \tag{B6}$$

on the proximitized dot, where $u > v$ in Eq. (B4), and $v > u$ in Eq. (B6). The precise choice of the corner in the CSD depends on (i) the choice of the degeneracy on the normal dot, and (ii) the choice of the ABS, i.e., $\varepsilon_A = \pm\sqrt{E^2_{\mathrm{ZA}} - \Delta_0^2}$. The choice of the normal dot degeneracy yields different low-energy Hamiltonians due to the different spin orientations that are relevant for the transition. For the right two corners, the normal dot orbital is spin-down, so we have

$$H_T \approx -t_{\mathrm{so}} c_\uparrow^\dagger d_\downarrow + t c_\downarrow^\dagger d_\downarrow + \mathrm{H.c.}$$
$$\approx -t_{\mathrm{so}} v \gamma_\downarrow d_\downarrow - t u \gamma_\downarrow^\dagger d_\downarrow + \mathrm{H.c.}, \tag{B7}$$

where we have used the Bogoliubov transformation

$$c_\uparrow^\dagger = u\gamma_\uparrow^\dagger + v\gamma_\downarrow, \quad c_\downarrow^\dagger = -u\gamma_\downarrow^\dagger + v\gamma_\uparrow. \tag{B8}$$

So we have

$$t_{\mathrm{eff}} = -tu, \quad \Delta_{\mathrm{eff}} = -t_{\mathrm{so}} v \tag{B9}$$

for both bottom-right and top-right corners. On the other hand, for the left two corners, the dot orbitals are spin-up states, giving

$$H_T \approx t^* c_\uparrow^\dagger d_\uparrow + t_{\mathrm{so}} c_\downarrow^\dagger d_\uparrow + \mathrm{H.c.}$$
$$\approx t^* v \gamma_\downarrow d_\uparrow - t_{\mathrm{so}} u \gamma_\downarrow^\dagger d_\uparrow. \tag{B10}$$

Thus

$$t_{\mathrm{eff}} = -t_{\mathrm{so}} u, \quad \Delta_{\mathrm{eff}} = t^* v. \tag{B11}$$

The choice of top or bottom corner depends on the choice of the ABS. In Fig. 8 we have depicted the different options in the parameter regimes relevant for the problem. Choosing the negative energy ABS ($\varepsilon_A = -\sqrt{E^2_{\mathrm{ZA}} - \Delta_0^2}$) yields $v > u$,

TABLE I. Definition of the corners visible in the charge-stability diagram, Fig. 2. The given constraints on u, v and t, t_{so} determine whether the corresponding corner in the charge-stability diagram is a viable sweet spot.

	Left Dot D: $\|\downarrow\uparrow\rangle$; $\|\downarrow\rangle$	Right Dot D: $\|\downarrow\rangle$; $\|0\rangle$
Top	$t > t_{so}$	$t < t_{so}$
Dot A: $u\|0\rangle + v\|\uparrow\downarrow\rangle$; $\|\downarrow\rangle$	$u > v$	$u > v$
Bottom	$t < t_{so}$	$t > t_{so}$
Dot A: $\|\downarrow\rangle$; $u\|0\rangle + v\|\uparrow\downarrow\rangle$	$u < v$	$u < v$
H_{DA}^{eff} terms	$t_{eff} = -t_{so}u$; $\Delta_{eff} = t^{\dagger}v$	$t_{eff} = -tu$; $\Delta_{eff} = -t_{so}v$

while it is the opposite ($u > v$) for the positive energy ABS. Finally, the availability of a corner to host a sweet spot depends on the relation between t and t_{so}. The main text discusses the behavior at the bottom-right sweet spot when $t > t_{so}$, a condition that needs to be satisfied for the bottom-right corner to be a viable sweet spot. The choice of corner is then determined by the ABS, i.e., for the bottom-right corner that is $\varepsilon_A = -\sqrt{E_{ZA}^2 - \Delta_0^2}$, which yields $v > u$. This is necessary to enable $|t_{eff}| = |\Delta_{eff}|$; see Eq. (B9). Choosing the opposite ABS, i.e., $\varepsilon_A = \sqrt{E_{ZA}^2 - \Delta_0^2}$, one switches from the bottom-right to the top-right corner. This corner, however, cannot host any sweet spot when $t > t_{so}$ since

$$u = \sqrt{\frac{1}{2}\left(1 + \sqrt{1 - \Delta_0^2/E_{ZA}^2}\right)} \overset{\frac{\Delta_0}{E_{ZA}} \nearrow 1}{\approx} \frac{\sqrt{2}}{2} + \frac{\sqrt{1 - \Delta_0^2/E_{ZA}^2}}{2} + \frac{\sqrt{2}}{8}\left(\frac{\Delta_0^2}{E_{ZA}^2} - 1\right), \tag{B12}$$

$$v = \sqrt{\frac{1}{2}\left(1 - \sqrt{1 - \Delta_0^2/E_{ZA}^2}\right)} \overset{\frac{\Delta_0}{E_{ZA}} \nearrow 1}{\approx} \frac{\sqrt{2}}{2} - \frac{\sqrt{1 - \Delta_0^2/E_{ZA}^2}}{2} + \frac{\sqrt{2}}{8}\left(\frac{\Delta_0^2}{E_{ZA}^2} - 1\right) \tag{B13}$$

showing that $u > v$ for $E_{ZA} > \Delta_0$ (see also Fig. 8). If, however, $t_{so} > t$, the constraint on u, v is inverted and the availability of the two corners flips. For clarity, we introduce the precise definitions by which we refer to the corners of the CSD in Table I. There, we list the participating, i.e., degenerate states, on the normal dot (dot D) and the proximitized dot (dot A). Furthermore, we give the conditions relevant for the existence of the sweet spot, e.g., that a bottom-right sweet spot becomes viable if both $v > u$ and $t > t_{so}$ are met.

APPENDIX C: FINITE CHARGING ENERGY U_{ABS} IN THE ANDREEV BOUND STATE

The main text discusses a configuration without charging energy on the ABS dot. Removing this constraint, we obtain the Hamiltonian on the ABS dot as

$$H_A = (\varepsilon - E_{ZA})c_{\downarrow}^{\dagger}c_{\downarrow} + (\varepsilon + E_{ZA})c_{\uparrow}^{\dagger}c_{\uparrow} + \Delta_0 c_{\uparrow}^{\dagger}c^{\dagger}\downarrow + U_{ABS}c_{\uparrow}^{\dagger}c_{\downarrow}^{\dagger}c\downarrow c\uparrow + \text{H.c.} \tag{C1}$$

in the electronic basis. U_{ABS} is the charging energy on the ABS, and the remaining symbols are defined in Sec. II A. In the many-body basis, $\{|0\rangle, |\downarrow\uparrow\rangle, |\downarrow\rangle, |\uparrow\rangle\}$, we can write the Hamiltonian

$$H_A = \begin{pmatrix} 0 & \Delta & 0 & 0 \\ \Delta & 2\varepsilon + U_{ABS} & 0 & 0 \\ 0 & 0 & \varepsilon - E_{ZA} & 0 \\ 0 & 0 & 0 & \varepsilon + E_{ZA} \end{pmatrix}. \tag{C2}$$

We substitute $\xi = 2\varepsilon + U_{ABS}$ and define $E_\xi = \sqrt{\xi^2 + \Delta^2}$. With these replacements, we can write the ground state of the even- and odd-parity subspaces as

$$E_{GS}^{(even)} = \xi - \sqrt{\xi^2 + \Delta^2},$$

$$|GS_{odd}\rangle = \sqrt{\frac{E_\xi + \xi}{2E_\xi}}|0\rangle + \sqrt{\frac{E_\xi - \xi}{2E_\xi}}|\uparrow\downarrow\rangle, \tag{C3}$$

$$E_{GS}^{(odd)} = \varepsilon - E_{ZA}, \quad |GS_{even}\rangle = |\downarrow\rangle. \tag{C4}$$

To induce MZMs on the dots, the two ground states need to be degenerate. They are connected through a quasiparticle excitation $|GS_{even}\rangle = (uc_{\downarrow}^{\dagger} - vc_{\uparrow}^{\dagger})|GS_{odd}\rangle$ with u, v to be determined. We obtain the condition

$$u\sqrt{\frac{E_\xi + \xi}{2E_\xi}} + v\sqrt{\frac{E_\xi - \xi}{2E_\xi}} = 1, \tag{C5}$$

which is solved by $u(U_{ABS}) = \sqrt{\frac{E_\xi + \xi}{2E_\xi}}$, $v(U_{ABS}) = \sqrt{\frac{E_\xi - \xi}{2E_x i}}$ since $u(U_{ABS})^2 + v(U_{ABS})^2 = 1$. The degeneracy condition requires

$$E_{GS}^{(even)} = E_{GS}^{(odd)} \tag{C6}$$

leading to ξ being constrained to

$$\xi^2 = \left(\frac{U_{ABS}}{2} + E_{ZA}\right)^2 - \Delta^2. \tag{C7}$$

To satisfy $v(U_{ABS}) > u(U_{ABS})$ (see Appendix B) we choose the negative root solution for ξ. Gathering all findings into $u(U_{ABS})$ and $v(U_{ABS})$, we can write

$$u(U_{ABS}) = \sqrt{\frac{E_\xi + \xi}{2E_\xi}} \overset{U_{ABS}\to 0}{\approx} u - \frac{u}{4}\frac{\Delta^2}{\xi_0 E_{ZA}(E_{ZA} - \xi_0)}U_{ABS}, \tag{C8}$$

$$v(U_{ABS}) = \sqrt{\frac{E_\xi - \xi}{2E_\xi}} \overset{U_{ABS}\to 0}{\approx} v + \frac{v}{4}\frac{\Delta^2}{\xi_0 E_{ZA}(E_{ZA} - \xi_0)}U_{ABS}, \tag{C9}$$

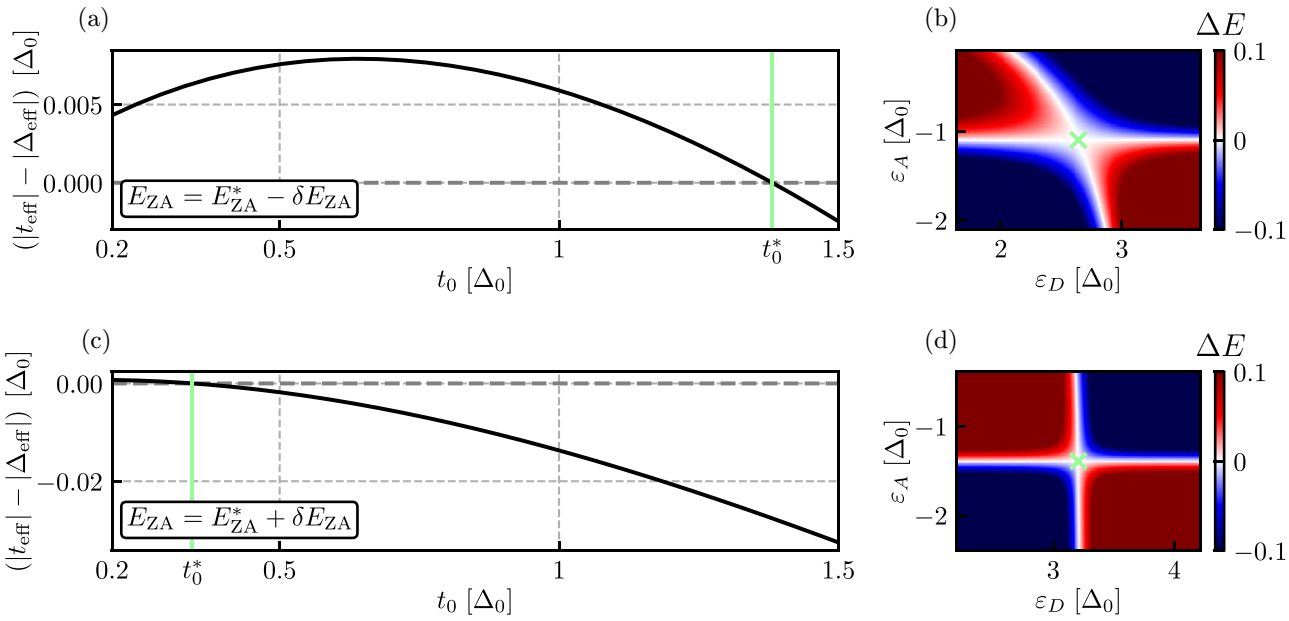

FIG. 9. Sweet spot recovery through adjustment of t_0. Panels (a) and (b) show how, when starting with $t_0 = 0.2$ but $E_{ZA} = E^*_{ZA} - \delta E_{ZA}$, a sweet spot can be recovered by increasing t_0. Particularly (b) demonstrates the corresponding $t_0 > \Delta_0$, strongly coupling the two dots. We lastly want to highlight that, despite the slope of $|t_{\text{eff}}| - |\Delta_{\text{eff}}|$ being negative towards smaller t_0 in (a), it is impossible to recover a sweet spot by decreasing the hopping further. Panels (c) and (d) demonstrate sweet spot recovery when $t_0 = 1.5$ initially and $E_{ZA} = E^*_{ZA} + \delta E_{ZA}$.

where we used $\xi_0 = \sqrt{E^2_{\text{ZA}} - \Delta^2}$, and u, v as defined in Sec. II A. We recognize that u decreases while v increases. It is therefore to be expected that the Zeeman energy at which the sweet spot is observed reduces. Indeed, we find E^*_{ZA} for $\theta = 0$ at the sweet spot as

$$E^*_{\text{ZA}} = \frac{\Delta_0}{\sin(2\alpha)} - \frac{U_{\text{ABS}}}{2}. \tag{C10}$$

Since two corners of the charge-stability diagram are roughly separated by $\simeq 2E_{ZA} + U_{\text{ABS}}$, a finite U_{ABS} can serve to help make the sweet spot more resilient towards single-parameter perturbations. Furthermore, Eq. (C10) shows that large enough U_{ABS} can push the sweet spot Zeeman energy below Δ_0. Hence, sweet spots can emerge even if $E_{ZA} < \Delta_0$ as a result of the separation of the ABS states in ε_A and Eq. (C10). This final property might be particularly useful when the platform inherent g-factor might be limited through other constraints.

APPENDIX D: CONTROLLING THE EFFECTIVE PAIRING THROUGH t_0

In Sec. II E we used a phenomenological pairing parameter Δ_D on the initially normal dot to demonstrate how a change on the pairing on the dot can recover a sweet spot. This Appendix builds upon Sec. II E, demonstrating explicitly on the many-body system how the induced pairing from the ABS is controlled through the bare hopping t_0. In particular, when the ABS dot is tuned slightly off the sweet spot in E_{ZA}, we can adjust t_0 to recover a sweet spot. Figure 9 demonstrates sweet spot recovery along two examples: (a) and (b) show how large t_0 recovers a sweet spot when starting with an initially small t_0 ($= 0.2$) and $E_{ZA} = E^*_{ZA} - \delta E_{ZA}$; (c) and (d) demonstrate recovery for small t_0 when beginning with $t_0 = 1.5$, i.e., strong coupling of the dots, at $E_{ZA} = E^*_{ZA} + \delta E_{ZA}$.

APPENDIX E: INHOMOGENEITY IN THE DOT-ABS ARRAY

In this Appendix, we consider the effect of Hamiltonian parameter inhomogeneity in a dot-ABS array. This captures the realistic situation of an experimental device. To demonstrate the main physical effect, we focus on the three-site Kitaev chain with four different scenarios: DAD and ADA with inhomogeneous spin-orbit interaction, and DAD and ADA with an inhomogeneous g-factor. Here we choose the level of inhomogeneity to be 10% to generate the results in Figs. 10 and 11, and we emphasize that our results are robust even for larger values. We find that the physical findings and main conclusions presented in the main text are still valid, e.g., the presence of long-range coupling between Majoranas with negligible wave-function overlap, and energy spectra against chemical potential detuning. In our simulation here, we need to first figure out the sweet spots in each two-site DA pair by varying the tunnel strength t_0. After that, the sweet spot of a three-site DA pair is obtained by putting them together. It is likely that the middle site (either dot or ABS) may reach different values of chemical potential for the left and right pairs, respectively, and we choose to take the average of them. In addition, to capture the proximity effect from the continuum states, we add a pairing term $\Delta_{D,\text{induced}} \approx t_0^2 \delta\Delta$ on normal quantum dots, with $\delta\Delta = 0.5\Delta_0$. We note that the induced gap is proportional to t_0^2 due to the second-order process of local Andreev reflection, and that $\delta\Delta$ is a phenomenological parameter that is proportional to the superconductor density

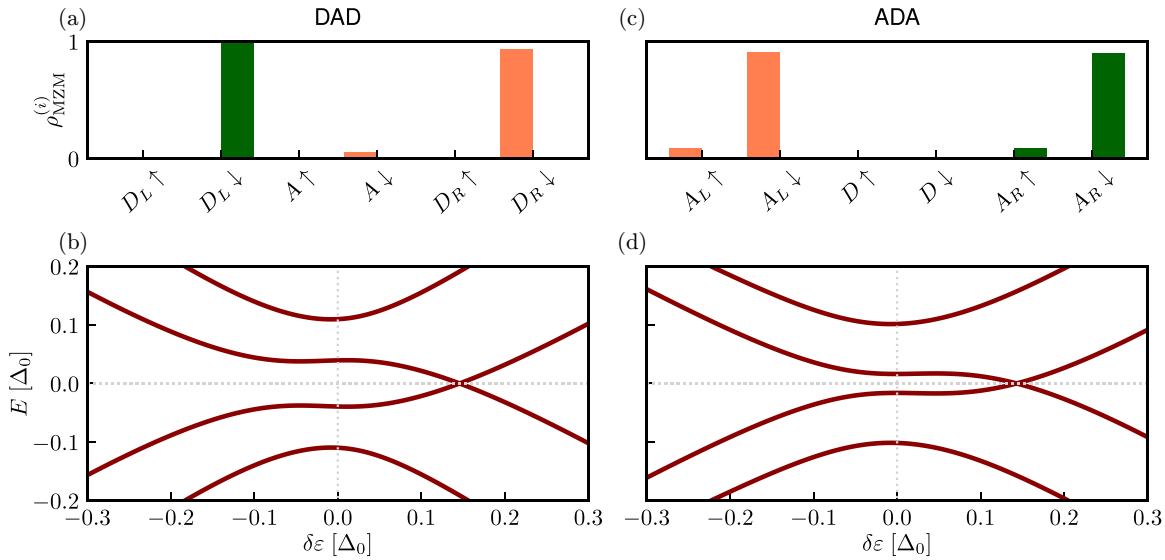

FIG. 10. Inhomogeneous spin-orbit interaction between the two pairs. We allow for a deviation of 10% between the different α_i ($\alpha_L = 0.3, \alpha_R = 0.27$). We see that the ADA setup reproduces the behavior suggested in the main text (d) despite the inhomogeneity and yields well separated Majoranas (c). This is explained by the better protection against next-nearest-neighbor hopping from the larger g-factor in the central, normal dot. The DAD setup, however, is more sensitive to changes of the chemical potential of the middle dot. The smaller g-factor in the ABS dot generally leads to poorer protection against next-nearest-neighbor hopping. Yet, we obtain still well separated Majoranas despite the sweet spot only being metastable against global changes of the chemical potential.

of states. We have checked that our simulation results do not depend on the precise value of $\delta\Delta$. To summarize, we have shown that even in the presence of parameter inhomogeneity, the sweet spot of an extended Kitaev chain can still be found by varying the tunnel strength between dot and ABS. Furthermore, the main findings presented in the main text are still valid.

1. Inhomogeneous spin-orbit interaction

We first consider inhomogeneous spin-orbit interaction in both ADA and DAD setups. We consider α_L and α_R, i.e., the spin-orbit interaction of the two pairs. The results of this analysis are depicted in Fig. 10. We recognize that, for both setups, we can well recover the spectral behavior discussed in Sec. III.

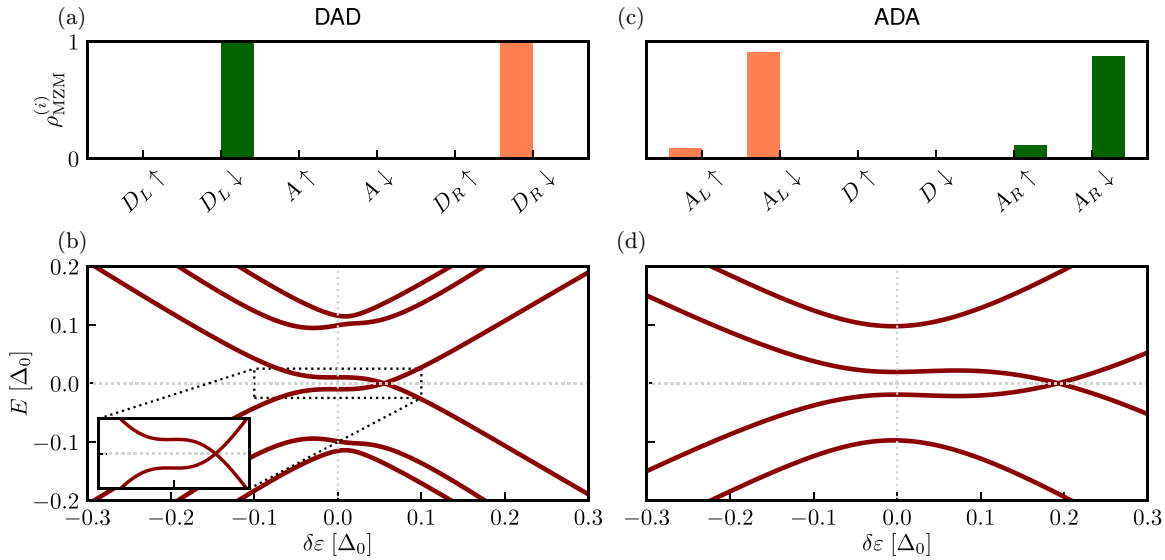

FIG. 11. Inhomogeneous g-factors between the dots. For the DAD setup, (a) and (b), we let the inhomogeneity be as large as 10% ($g_L = 2, g_R = 1.8$). We find that, despite the stark difference, the spectrum reproduces the findings of the main text well and the Majoranas yielded by the system are well separated from each other. This resilience is due to the larger level separation of the levels on the normal dots. For the ADA setup we allow for an inhomogeneity of 10% ($g_L = 1, g_R = 0.9$). In both cases, we recover spectral lines akin to those demonstrated in the main text despite the presence of inhomogeneities. Consequently, also the Majorana wave functions remain well separated between the dots.

Furthermore, we see that the Majorana wave functions shown in Figs. 10(a) and 10(c) are still well separated.

2. Inhomogeneous *g*-factor

Lastly, we consider inhomogeneous g-factors between the dots. The different g-factors of the outer dots between the two setups make them differently susceptible to inhomogeneities of the g-factor. We choose $g_L = 2$, $g_R = 1.8$ for the DAD and $g_L = 1$, $g_R = 0.9$ for the ADA setup. This choice yields reasonably different sweet spots of the two pairs of two-site chains that can still be connected by barrier tuning of the second pair, i.e., varying t_0. The results of this analysis are depicted in Fig. 11. For both situations, we find that the behavior of the spectrum suggested in the main text can still be reasonably well reproduced and that the Majoranas that the systems yield are still well separated.

[1] A. Y. Kitaev, Unpaired Majorana fermions in quantum wires, Phys. Usp. **44**, 131 (2001).

[2] J. Alicea, New directions in the pursuit of Majorana fermions in solid state systems, Rep. Prog. Phys. **75**, 076501 (2012).

[3] M. Leijnse and K. Flensberg, Introduction to topological superconductivity and Majorana fermions, Semicond. Sci. Technol. **27**, 124003 (2012).

[4] C. W. J. Beenakker, Search for Majorana fermions in superconductors, Annu. Rev. Condens. Matter Phys. **4**, 113 (2013).

[5] T. D. Stanescu and S. Tewari, Majorana fermions in semiconductor nanowires: Fundamentals, modeling, and experiment, J. Phys.: Condens. Matter **25**, 233201 (2013).

[6] J.-H. Jiang and S. Wu, Non-Abelian topological superconductors from topological semimetals and related systems under the superconducting proximity effect, J. Phys.: Condens. Matter **25**, 055701 (2013).

[7] S. R. Elliott and M. Franz, Colloquium: Majorana fermions in nuclear, particle, and solid-state physics, Rev. Mod. Phys. **87**, 137 (2015).

[8] M. Sato and S. Fujimoto, Majorana fermions and topology in superconductors, J. Phys. Soc. Jpn. **85**, 072001 (2016).

[9] M. Sato and Y. Ando, Topological superconductors: A review, Rep. Prog. Phys. **80**, 076501 (2017).

[10] R. Aguado, Majorana quasiparticles in condensed matter, Riv. Nuovo Cimento **40**, 523 (2017).

[11] R. M. Lutchyn, E. P. A. M. Bakkers, L. P. Kouwenhoven, P. Krogstrup, C. M. Marcus, and Y. Oreg, Majorana zero modes in superconductor–semiconductor heterostructures, Nat. Rev. Mater. **3**, 52 (2018).

[12] H. Zhang, D. E. Liu, M. Wimmer, and L. P. Kouwenhoven, Next steps of quantum transport in Majorana nanowire devices, Nat. Commun. **10**, 5128 (2019).

[13] S. M. Frolov, M. J. Manfra, and J. D. Sau, Topological superconductivity in hybrid devices, Nat. Phys. **16**, 718 (2020).

[14] D. A. Ivanov, Non-abelian statistics of half-quantum vortices in p-wave superconductors, Phys. Rev. Lett. **86**, 268 (2001).

[15] C. Nayak, S. H. Simon, A. Stern, M. Freedman, and S. Das Sarma, Non-Abelian anyons and topological quantum computation, Rev. Mod. Phys. **80**, 1083 (2008).

[16] S. D. Sarma, M. Freedman, and C. Nayak, Majorana zero modes and topological quantum computation, npj Quantum Inf. **1**, 15001 (2015).

[17] S. Plugge, A. Rasmussen, R. Egger, and K. Flensberg, Majorana box qubits, New J. Phys. **19**, 012001 (2017).

[18] T. Karzig, C. Knapp, R. M. Lutchyn, P. Bonderson, M. B. Hastings, C. Nayak, J. Alicea, K. Flensberg, S. Plugge, Y. Oreg, C. M. Marcus, and M. H. Freedman, Scalable designs for quasiparticle-poisoning-protected topological quantum computation with Majorana zero modes, Phys. Rev. B **95**, 235305 (2017).

[19] J. D. Sau, R. M. Lutchyn, S. Tewari, and S. Das Sarma, Generic new platform for topological quantum computation using semiconductor heterostructures, Phys. Rev. Lett. **104**, 040502 (2010).

[20] R. M. Lutchyn, J. D. Sau, and S. Das Sarma, Majorana fermions and a topological phase transition in semiconductor-superconductor heterostructures, Phys. Rev. Lett. **105**, 077001 (2010).

[21] Y. Oreg, G. Refael, and F. von Oppen, Helical liquids and Majorana bound states in quantum wires, Phys. Rev. Lett. **105**, 177002 (2010).

[22] V. Mourik, K. Zuo, S. M. Frolov, S. R. Plissard, E. P. A. M. Bakkers, and L. P. Kouwenhoven, Signatures of Majorana fermions in hybrid superconductor-semiconductor nanowire devices, Science **336**, 1003 (2012).

[23] M. T. Deng, S. Vaitiekenas, E. B. Hansen, J. Danon, M. Leijnse, K. Flensberg, J. Nygård, P. Krogstrup, and C. M. Marcus, Majorana bound state in a coupled quantum-dot hybrid-nanowire system, Science **354**, 1557 (2016).

[24] F. Pientka, A. Keselman, E. Berg, A. Yacoby, A. Stern, and B. I. Halperin, Topological superconductivity in a planar josephson junction, Phys. Rev. X **7**, 021032 (2017).

[25] M. Hell, M. Leijnse, and K. Flensberg, Two-dimensional platform for networks of Majorana bound states, Phys. Rev. Lett. **118**, 107701 (2017).

[26] A. Fornieri, A. M. Whiticar, F. Setiawan, E. Portolés, A. C. C. Drachmann, A. Keselman, S. Gronin, C. Thomas, T. Wang, R. Kallaher, G. C. Gardner, E. Berg, M. J. Manfra, A. Stern, C. M. Marcus, and F. Nichele, Evidence of topological superconductivity in planar josephson junctions, Nature (London) **569**, 89 (2019).

[27] P. M. R. Brydon, S. Das Sarma, H.-Y. Hui, and J. D. Sau, Topological Yu-Shiba-Rusinov chain from spin-orbit coupling, Phys. Rev. B **91**, 064505 (2015).

[28] S. Nadj-Perge, I. K. Drozdov, J. Li, H. Chen, S. Jeon, J. Seo, A. H. MacDonald, B. A. Bernevig, and A. Yazdani, Observation of Majorana fermions in ferromagnetic atomic chains on a superconductor, Science **346**, 602 (2014).

[29] G. Kells, D. Meidan, and P. W. Brouwer, Near-zero-energy end states in topologically trivial spin-orbit coupled

superconducting nanowires with a smooth confinement, Phys. Rev. B **86**, 100503(R) (2012).

[30] E. Prada, P. San-Jose, and R. Aguado, Transport spectroscopy of *NS* nanowire junctions with Majorana fermions, Phys. Rev. B **86**, 180503(R) (2012).

[31] C.-X. Liu, J. D. Sau, T. D. Stanescu, and S. Das Sarma, Andreev bound states versus Majorana bound states in quantum dot-nanowire-superconductor hybrid structures: Trivial versus topological zero-bias conductance peaks, Phys. Rev. B **96**, 075161 (2017).

[32] C. Moore, T. D. Stanescu, and S. Tewari, Two-terminal charge tunneling: Disentangling majorana zero modes from partially separated Andreev bound states in semiconductor-superconductor heterostructures, Phys. Rev. B **97**, 165302 (2018).

[33] C. Reeg, O. Dmytruk, D. Chevallier, D. Loss, and J. Klinovaja, Zero-energy Andreev bound states from quantum dots in proximitized Rashba nanowires, Phys. Rev. B **98**, 245407 (2018).

[34] A. Vuik, B. Nijholt, A. R. Akhmerov, and M. Wimmer, Reproducing topological properties with quasi-Majorana states, SciPost Phys. **7**, 061 (2019).

[35] H. Pan and S. Das Sarma, Physical mechanisms for zero-bias conductance peaks in Majorana nanowires, Phys. Rev. Res. **2**, 013377 (2020).

[36] J. D. Sau and S. D. Sarma, Realizing a robust practical Majorana chain in a quantum-dot-superconductor linear array, Nat. Commun. **3**, 964 (2012).

[37] M. Leijnse and K. Flensberg, Parity qubits and poor man's Majorana bound states in double quantum dots, Phys. Rev. B **86**, 134528 (2012).

[38] T. Dvir, G. Wang, N. van Loo, C.-X. Liu, G. P. Mazur, A. Bordin, S. L. D. ten Haaf, J.-Y. Wang, D. van Driel, F. Zatelli, X. Li, F. K. Malinowski, S. Gazibegovic, G. Badawy, E. P. A. M. Bakkers, M. Wimmer, and L. P. Kouwenhoven, Realization of a minimal Kitaev chain in coupled quantum dots, Nature (London) **614**, 445 (2023).

[39] C.-X. Liu, G. Wang, T. Dvir, and M. Wimmer, Tunable superconducting coupling of quantum dots via Andreev bound states in semiconductor-superconductor nanowires, Phys. Rev. Lett. **129**, 267701 (2022).

[40] A. Bordin, G. Wang, C.-X. Liu, S. L. D. ten Haaf, N. van Loo, G. P. Mazur, D. Xu, D. van Driel, F. Zatelli, S. Gazibegovic, G. Badawy, E. P. A. M. Bakkers, M. Wimmer, L. P. Kouwenhoven, and T. Dvir, Tunable crossed Andreev reflection and elastic cotunneling in hybrid nanowires, Phys. Rev. X **13**, 031031 (2023).

[41] G. Wang, T. Dvir, G. P. Mazur, C.-X. Liu, N. van Loo, S. L. D. ten Haaf, A. Bordin, S. Gazibegovic, G. Badawy, E. P. A. M. Bakkers, M. Wimmer, and L. P. Kouwenhoven, Singlet and triplet Cooper pair splitting in hybrid superconducting nanowires, Nature (London) **612**, 448 (2022).

[42] Q. Wang, S. L. D. ten Haaf, I. Kulesh, D. Xiao, C. Thomas, M. J. Manfra, and S. Goswami, Triplet correlations in Cooper pair splitters realized in a two-dimensional electron gas, Nat. Commun. **14**, 4876 (2023).

[43] A. Tsintzis, R. S. Souto, and M. Leijnse, Creating and detecting poor man's Majorana bound states in interacting quantum dots, Phys. Rev. B **106**, L201404 (2022).

[44] I. C. Fulga, A. Haim, A. R. Akhmerov, and Y. Oreg, Adaptive tuning of Majorana fermions in a quantum dot chain, New J. Phys. **15**, 045020 (2013).

[45] W. Samuelson, V. Svensson, and M. Leijnse, Minimal quantum dot based Kitaev chain with only local superconducting proximity effect, Phys. Rev. B **109**, 035415 (2024).

[46] T. D. Stanescu, J. D. Sau, R. M. Lutchyn, and S. Das Sarma, Proximity effect at the superconductor-topological insulator interface, Phys. Rev. B **81**, 241310(R) (2010).

[47] C. Reeg, D. Loss, and J. Klinovaja, Metallization of a Rashba wire by a superconducting layer in the strong-proximity regime, Phys. Rev. B **97**, 165425 (2018).

[48] A. E. Antipov, A. Bargerbos, G. W. Winkler, B. Bauer, E. Rossi, and R. M. Lutchyn, Effects of gate-induced electric fields on semiconductor Majorana nanowires, Phys. Rev. X **8**, 031041 (2018).

[49] J. D. S. Bommer, H. Zhang, Ö. Gül, B. Nijholt, M. Wimmer, F. N. Rybakov, J. Garaud, D. Rodic, E. Babaev, M. Troyer, D. Car, S. R. Plissard, E. P. A. M. Bakkers, K. Watanabe, T. Taniguchi, and L. P. Kouwenhoven, Spin-orbit protection of induced superconductivity in Majorana nanowires, Phys. Rev. Lett. **122**, 187702 (2019).

[50] C.-X. Liu, J. D. Sau, T. D. Stanescu, and S. Das Sarma, Conductance smearing and anisotropic suppression of induced superconductivity in a Majorana nanowire, Phys. Rev. B **99**, 024510 (2019).

[51] Y. Luh, Bound state in superconductors with paramagnetic impurities, Acta Phys. Sin. **21**, 75 (1965).

[52] H. Shiba, Classical spins in superconductors, Prog. Theor. Phys. **40**, 435 (1968).

[53] A. I. Rusinov, Theory of gapless superconductivity in alloys containing paramagnetic impurities, Sov. Phys. JETP **29**, 1101 (1969).

[54] K. Grove-Rasmussen, G. Steffensen, A. Jellinggaard, M. H. Madsen, R. Žitko, J. Paaske, and J. Nygård, Yu–Shiba–Rusinov screening of spins in double quantum dots, Nat. Commun. **9**, 2376 (2018).

[55] H. Pan and S. Das Sarma, Majorana nanowires, Kitaev chains, and spin models, Phys. Rev. B **107**, 035440 (2023).

[56] F. Zatelli, D. van Driel, D. Xu, G. Wang, C.-X. Liu, A. Bordin, B. Roovers, G. P. Mazur, N. van Loo, J. C. Wolff *et al.*, Robust poor man's Majorana zero modes using Yu-Shiba-Rusinov states, arXiv:2311.03193.

[57] S. Miles, D. van Driel, M. Wimmer, and C.-X. Liu, Kitaev chain in an alternating quantum dot-Andreev bound state array (2023) doi: 10.5281/zenodo.8378441.

[58] I. A. Day, S. Miles, H. K. Kerstens, D. Varjas, and A. R. Akhmerov, Pymablock: An algorithm and a package for quasi-degenerate perturbation theory, arXiv:2404.03728.